Wind and Structures, *Vol. 35, No. 5 (2022) 337-351*
https://doi.org/10.12989/was.2022.35.5.337

Aerodynamic shape optimization emphasizing static stability for a super-long-span cable-stayed bridge with a central-slotted box deck

Ledong Zhu[1,2,3], Cheng Qian[1,2,3], Yikai Shen[4] and Qing Zhu*[1,2.3]

[1]*State Key Laboratory of Disaster Reduction in Civil Engineering, Tongji University, Shanghai 200092, China*
[2]*Department of Bridge Engineering, Tongji University, Shanghai 200092, China*
[3]*Key Laboratory of Transport Industry of Bridge Wind Resistance Technology, Tongji University, Shanghai 200092, China*
[4]*Shanghai Research Institute of Building Sciences, Shanghai 200092, China*

(*Received March 18, 2021, Revised September 20, 2022, Accepted September 22, 2022*)

Abstract. As central-slotted box decks usually have excellent flutter performance, studies on this type of deck mostly focus on the vortex-induced vibration (VIV) control. Yet with the increasing span lengths, cable-supported bridges may have critical wind speeds of wind-induced static instability lower than that of the flutter. This is especially likely for bridges with a central-slotted box deck. As a result, the overall aerodynamic performance of such a bridge will depend on its wind-induced static stability. Taking a 1400 m-main-span cable-stayed bridge as an example, this study investigates the influence of a series of deck shape parameters on both static and flutter instabilities. Some crucial shape parameters, like the height ratio of wind fairing and the angle of the inner-lower web, show opposite influences on the two kinds of instabilities. The aerodynamic shape optimization conducted for both static and flutter instabilities on the deck based on parameter-sensitivity studies raises the static critical wind speed by about 10%, and the overall critical wind speed by about 8%. Effective VIV countermeasures for this type of bridge deck have also been proposed.

Keywords: aerodynamic shape optimization; central-slotted box deck; flutter; super-long-span cable-stayed bridge; vortex-induced vibration; wind-induced static stability

1. Introduction

Modern cable-stayed bridges are recognized as having great crossing capacity ranking only next to suspension bridges and has been rapidly developed since the 1990s. Cable-stayed bridges entered a new era with main spans over 1000 m since the erection of the Sutong Bridge over the Yangtze River with a main span of 1088 m in 2007. Soon after, the Stonecutters Bridge in Hong Kong with a main span of 1018 m was built in 2008, and the Russky Island Bridge with a main span of 1104m was constructed later in 2012. More recently, the Hutong Bridge over the Yangtze River, a road-rail bridge with a main span of 1092m, was completed in 2019. The study by Gimsing and Georgakis (2012) on the ultimate span length of cable-stayed bridges has demonstrated that they are economically competitive with suspension bridges for span lengths between 1200 to 1500 m. The studies conducted by Nagai *et al.* (2004) and Zhu *et al.* (2011) have concluded that a 1400m-main-span cable-stayed bridge with a closed-box deck is aerodynamically feasible, even for typhoon-prone regions with wind speeds over 80m/s. Zhang and Sun (2014)'s study has shown that compared to a suspension bridge with a similar main span, a cable-stayed bridge has larger structural stiffness and thus higher static stability.

As cable-stayed bridges become more flexible and sensitive to the wind with increasing span lengths, the performances against wind-induced static and dynamic instabilities become critical problems controlling the design. Further, with the increasing span lengths, the critical wind speeds of wind-induced static instability of cable-stayed bridges can become close to or even lower than that of flutter instability. Wind-induced static instability is traditionally divided into lateral-torsional buckling and torsional divergence according to the mode of instability. But both of them are static instability with sudden large wind-induced torsional deformations at a certain high wind speed. With the development of advanced nonlinear finite element analyses on this issue, it has been found that the instability mode of modern long-span cable-stayed bridges is usually coupled with multiple degrees of freedom (DOFs). Hirai *et al.* (1967) have observed static divergence of a suspension bridge in the wind tunnel tests of an aeroelastic full-bridge model. Kien *et al.* (2007) investigated the static and dynamic wind-induced instability of super-long-span cable-stayed bridges with main span lengths of 1200 to 1800 m. The results show that span lengths are mainly constrained by static instability, and safety against both static and dynamic instabilities can be ensured even with a main span length of 1800 m. When Zhu *et al.* (2011) studied the scheme of a steel box girder cable-stayed bridge with a span of 1400 m, they found that the wind-induced static instability occurred before the flutter for the angles of attack (AoAs) of 0° and +3°, respectively with torsional displacements of 2.1° and 5.0° just prior to the observed instabilities. Hu *et al.* (2019) investigated the

*Corresponding author, Ph.D.
E-mail: zhuqing@tongji.edu.cn

Copyright © 2022 Techno-Press, Ltd.

ISSN: 1226-6116 (Print), 1598-6225 (Online)

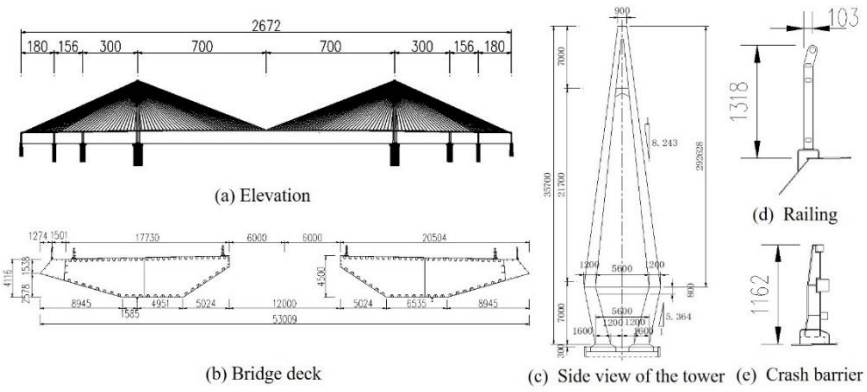

Fig. 1 Layout of the preliminary design scheme of the cable-stayed bridge with a main span of 1400 m

relative relations between wind-induced static instability and flutter instability in a cable-stayed bridge with double main spans of 1500 m and studied the influences of bridge deck types on the relative relationship between these two instabilities. For a typical box girder, the influence of shape parameters on the wind-induced static stability has also been investigated (Jiang *et al*. 2019).

Centrally slotting a fully-closed box deck can remarkably enhance the flutter critical wind speeds of long-span bridges (Larsen and Astiz 1998, Sato *et al*. 2002, Sato *et al.* 2000, Yang *et al*. 2018) and has been adopted in world record-breaking bridges such as the Xihoumen suspension bridge (2009, China), with a main span of 1650 m, the Yi Sun-sin suspension bridge (2012, South Korea), 1545 m and the Çanakkale1915 suspension bridge (2022, Turkey), 2023 m. Sato *et al.* (2000) investigated the effect of slotting ratio on the flutter performance of streamlined flat box girder with an aspect ratio of 17 and found that the critical wind speed always presents an increasing trend with the slotting ratio increasing from 0% to 100%. Yang *et al.* (2007) pointed out that central slotting of the main beam is beneficial to the flutter performance of the streamlined section, but unfavorable to that of more bluff non-flat streamlined section. Further, taking Xihoumen cross-sea bridge as the background, Yang *et al.* (2015b) studied the influence of slotting ratio and wind fairing form on flutter performance. They found that the critical wind speed increases first and then decreases with the increase of slotting rate, and reaches the maximum when the slotting ratio is 40%.

However, the central grooving of a box girder may intensify the vortex shedding around the girder and cause vortex-induced vibrations (Li *et al*. 2011, Liu *et al*. 2021). The aerodynamic control measure of VIV on this type of bridge is, therefore, a hot research topic.(Larsen 1993, Larsen *et al*. 2008, Yang *et al*. 2015b) studied the effects of aerodynamic measures such as the wind fairing form and the guide plate on the inhibition of VIV.

The current studies on this type of deck mostly focus on its VIV performance and control. Only a limited body of research can be found on its wind-induced static stability(Yang *et al*. 2015b). Wind-induced static instability of long-span bridges may cause an abrupt overturning of the bridge deck, and is thus more dangerous than flutter. In this connection, it is reasonable to design a bridge with a critical wind speed of wind-induced instability higher than that of the flutter. Otherwise, the high flutter-resistance capacity of a central-slotted box deck would be superfluous.

Table 1 Fundamental frequencies and modal masses of the bridge

	1st longitudinal	1st symmetric lateral bending	1st symmetric vertical bending	1st symmetric torsion
f (Hz)	0.074	0.093	0.154	0.398
m_{eq}(t/m) or J_{meq} (t·m^2/m)	59.83	33.06	37.95	10320

Taking a 1400 m-main-span cable-stayed bridge as an example, this study investigates the influence of a series of deck shape parameters on both static and flutter instabilities, emphasizing the former. The aerodynamic shape optimization based on parameter-sensitivity studies is conducted for both static and flutter instabilities on the deck. The VIV performance and countermeasures for this type of bridge deck is also studied.

2. Introduction to the objective bridge scheme

In this study, the preliminary design scheme of a cable-stayed bridge with a main span of 1400 m and a central-slotted box deck, as shown in Fig. 1, is taken as the background case to investigate the aerodynamic shape Fig. 1(a) shows the elevation of the general layout. The total length of the bridge is 2672 m. Fig. 1(b) shows the preliminary design of the deck cross-section. Two boxes share a width of 20.5 m are separated by a central slot of 12.0m. The central height of the deck is 4.5 m. 357 m high A-shape PC towers, as shown in Fig. 1(c), are employed. Table 1 lists the computed natural frequencies (f) of the fundamental modes and the corresponding equivalent mass (m_{eq}), or the inertia moment of mass (J_{meq}).

The critical wind speeds for the wind-induced static instability of the preliminary scheme were obtained with full-bridge static instability analyses with aerodynamic coefficients acquired from wind-tunnel tests. The analysis considers the geometric nonlinearities as well as the deformation-dependent wind loads. The solution procedure consists of three core parts: internal iteration, external

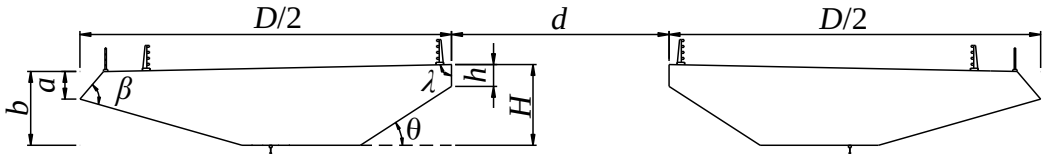

Fig. 2 Schematic diagram for the shape parameters

Table 2 Shape parameters for optimization

Shape parameters	Expression	Initial value	Values for investigation
height ratio of wind fairing	*a/b*	0.37	0.00, 0.20, 0.27, 0.37, 0.53, 0.56, 0.60, 0.67
height ratio of inner-upper web	*h/H*	0.27	0.27, 0.64, 1.00
slotting ratio	*d/D*	30%	20.0%, 30.0%, 40.0%
angle of inner-side lower web	θ	33°	16°, 22°, 28°, 33°
angle of wind fairing apex	β	66°	40°, 50°, 66°

iteration and automatic update of the wind speed. At each wind velocity increment, the internal cycle of iteration is performed to solve the nonlinear structural response by using the Newton-Raphson method. Then, the external cycle of iteration is performed to obtain the equilibrium of the additional wind load and the structural response. Finally, an automatically updated wind speed upper limit is set to optimize the wind speed increment. More details about the solution procedure can be found in Qian *et al.* (2022). The resulting critical wind speeds are 124.5 m/s, 129.4 m/s and 122.0 m/s, respectively, for initial AoAs of -3°, 0° and 3°. The critical wind speed of flutter, obtained by wind-tunnel flutter tests with a spring-mounted sectional model, is 161.5 m/s, which occurs at AoAs of 3°, and is 30% higher than that of the static instability.

The preliminary scheme of the bridge exhibits high aerodynamic performance because the design of the deck shape is based on existing super-long-span bridges. Yet as the conventional aerodynamic design of the deck shape mainly focuses on its flutter performance, the bridge has a critical wind speed of static instability far lower than that of flutter. The excellent against-flutter potential of the deck shape is superfluous for the overall critical wind speed of 122.0 m/s. Further, the current design of the deck shape may not provide sufficient critical wind speed for further longer bridge spans.

To improve the overall aerodynamic performance of the deck section, an aerodynamic shape optimization emphasizing static stability has been conducted.

3. Shape optimization for synthesis aerodynamic performance

3.1 Deck shape parameters

Six geometry parameters as shown in Fig. 2 and listed in Table 2 were chosen for the optimization of the aerodynamic shape. They are the height ratio of wind fairing (*a/b*), the height ratio of the inner- upper web (*h/H*), the slotting ratio (*d/D*), the angle of wind fairing (β), the angle of the inner-lower web(θ). The investigated values of these parameters are given in Table 2. Note that the width of the upper decks remains consistent as other parameters change, while the width of the lower deck is associated with the changing parameters.

3.2 Influence of shape parameters on aerodynamic coefficients and static stability

3.2.1 Obtaining aerodynamic coefficients and critical wind speed of static instability

To evaluate the critical wind speed of the wind-induced static instability, the aerodynamic coefficients of lift, drag and pitching moment need to be obtained via sectional

model tests of force measurement (Fig. 3). The tests were carried out in TJ-2 Wind Tunnel. To ensure a sufficient length-to-width ratio and a reasonable blocking ratio for such a wide deck, the geometric length scale (λ_L) is set to be 1/120. The sectional model is comprised of a measurement segment and a dummy segment with a 1mm-wide gap in between. The length, width and height of both segments are 0.645 m, 0.442 m, and 0.037 m, respectively. The testing wind speed is 7.5m/s, with a corresponding Reynolds number of 3.4×10^5. The tested AoAs are from -20° to 20°, with intervals of 1°.

The aerodynamic coefficients of drag, lift, and moment coefficients (C_D, C_L, C_M) are defined as follows

$$F_D = \frac{1}{2}\rho U^2 H C_D$$
$$F_L = \frac{1}{2}\rho U^2 B C_L \quad (1)$$
$$M_T = \frac{1}{2}\rho U^2 B^2 C_M$$

where U is the wind speed; ρ is the air density; F_D, F_L and M_T are the drag force, lift force, and torsional moment per unit length, respectively. The positive directions of aerodynamic forces as shown in Fig. 4.

Three-dimensional nonlinear wind-induced static instability analysis can then be conducted by a conventional

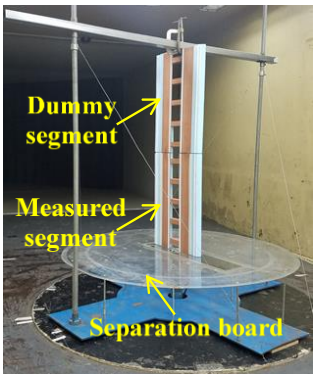

Fig. 3 Sectional model and force balance installed in TJ-2 Wind Tunnel

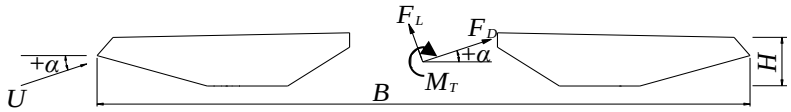

Fig. 4 Positive directions of the aerodynamic drag, lift and torsional moment

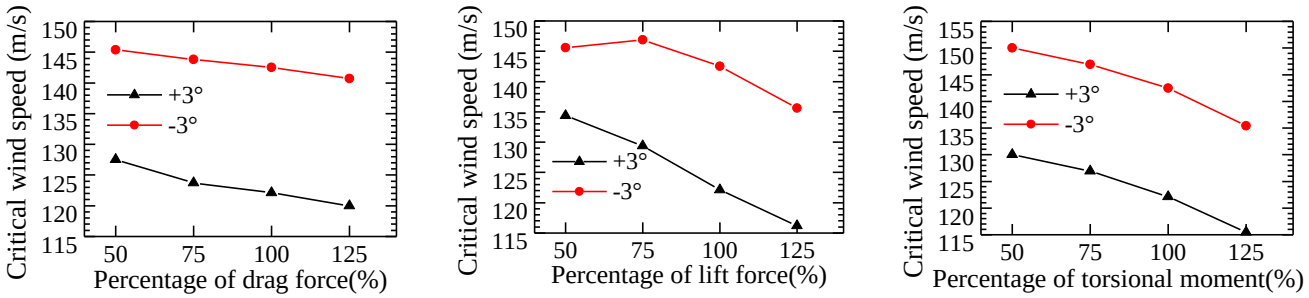

(a) Drag force (b) Lift force (c) Torsional moment

Fig. 5 Influence of aerodynamic coefficients on the critical wind speed for wind-induced static instability

Table 3 Cross sections with different *a*/*b*

a/*b*	Section Shape	*a*/*b*	Section Shape
0		0.37	
0.2		0.53	
0.27		0.67	

Note: h/H=0.27, θ=33°, λ=90°, d/D=30%. The width of the bottom plate is fixed. β is 66° except the case of a/b=0

method (Boonyapinyo *et al*. 1994, Cheng *et al*. 2002, Qian *et al*. 2022). The drag coefficient of cables was taken as 0.8. The aerodynamic coefficients of tower and pier elements were approximately determined according to the Chinese code. The wind speed profile was supposed to comply with the power-law with an exponent value of 0.12.

3.2.2 Influence of aerodynamic coefficients on wind-induced static instability

To study the influence of aerodynamic coefficients on the wind-induced static stability of this bridge before evaluation of each shape parameter, the coefficients were set as 0.5, 0.75 and 1.25 times their real values. Analyses for the critical wind speed of static instability for +3° and –3° angles of attack were carried out with these modified coefficients and the results are shown in Fig. 5 together with those with the real values. The influence of the drag and moment on the critical wind speed is approximately linear and exhibit similar patterns for both AoAs. When the drag and moment coefficients increase from 50% to 125%, the critical wind speed drops about 5m/s and 15m/s, respectively. The influence of lift force on the critical wind speed is highly associated with the AoA. When the lift coefficient increases from 50% to 125%, the critical wind speed drops about 8m/s and 18m/s for the -3° and +3° AoAs, respectively. The coefficients of the aerodynamic lift and torsional moment play crucial roles in the wind-induced stability instability of super-long-span cable-stayed bridges,

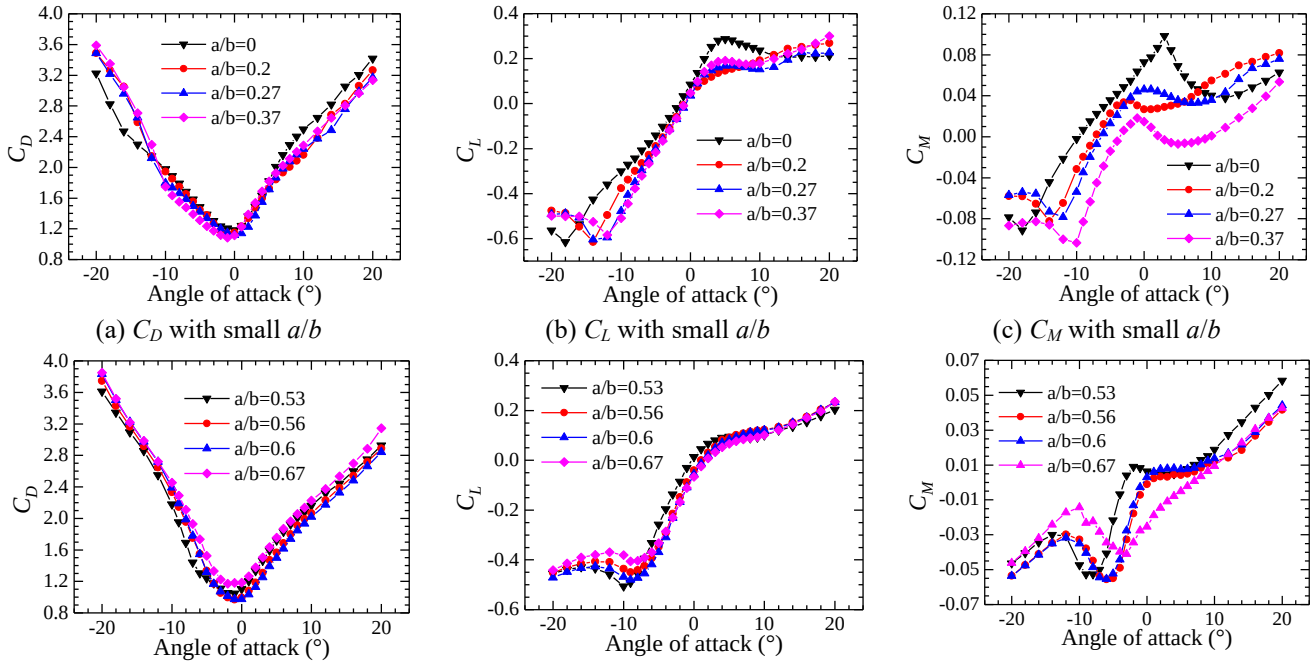

(a) C_D with small a/b (b) C_L with small a/b (c) C_M with small a/b

(d) C_D with large a/b (e) C_L with large a/b (f) C_M with large a/b

Fig. 6 Aerodynamic three-component coefficients C_L, C_D and C_M for sections with various a/b ratio

whilst the influence of the drag coefficient is comparatively small. The results indicate that the static instability is mainly driven by the torsion due to the aerodynamic moment and the reduction in structural stiffness due to the lift.

3.2.3 Influence of wind fairing apex (a/b)

Section shapes with different a/b are shown in Table 3. The influence of a/b on the aerodynamic coefficients are shown in Fig. 6. The change of a/b has little effect on the C_D. For a/b from 0.2 to 0.67, its influence on the C_L is also marginal. However, the change of a/b has a crucial influence on the C_M. For a/b smaller than 0.37 and the AoA greater than -10°, C_M decreases with the increase of a/b. For a/b greater than 0.53, C_M decreases with the increase of a/b only when the AoA is greater than -3°. When the AoA is smaller than -3°, C_M is always negative and generally decreases with the increase of a/b.

The results of the tested critical wind speeds for different a/b and AoAs are given in Fig. 7. The minimum critical wind speed of all sections occurs at +3° AoA.

The critical wind speeds at the AoAs of +3°, 0° and -3° increase with the increase of a/b, which means that the increase of a/b of the main girder section is beneficial to the wind-induced static stability. In practice, the section parameter a/b can be adjusted as an effective measure to improve the wind-induced static stability of cable-stayed bridges. When a/b changes from 0 to 0.67, the critical wind speed increases from 106.3m/s to 134.4 m/s.

3.2.4 Influence of height ratio of inner upper web (h/H)

The inclined angle of the inner lower web (θ) was kept constant while the change of h/H was investigated. Sections

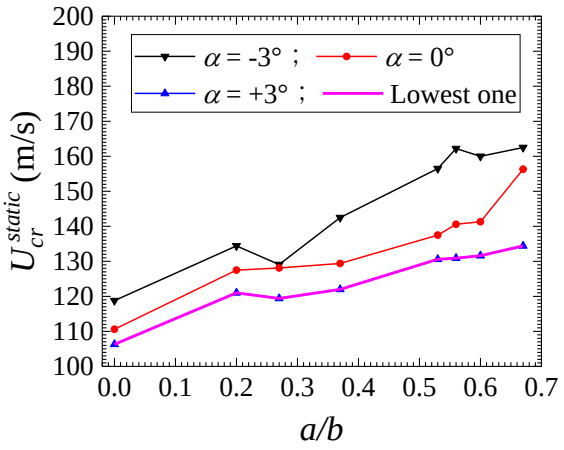

Fig. 7 Critical wind speeds for wind-induced static instability for sections with various a/b ratio

with h/H =0.27, 0.64 and 1 are selected for study while a/b were set as 0.37 and 0.53 respectively. Section shapes of various h/H with a/b=0.37 are shown in Table 4.

The influence of h/H on the aerodynamic coefficients are shown in Fig. 8. The h/H value has little effect on the C_D or C_L for both values of a/b. When a/b=0.37, C_M generally increases with h/H. When a/b=0.37, an obvious change in the

C_M due to different h/H can only be observed when the AoA is greater than 2°. The influence of h/H on C_M becomes larger as the absolute value of the AoA increases.

The results of the tested critical wind speeds for different h/H and AoAs are shown in Fig. 9. For a/b =0.37 and 0.53, the minimum critical wind speeds decrease from 122 m/s and 130.6 m/s to 115 m/s and 121.3 m/s, respectively, with the increase of h/H from 0.27 to 1.0.

Table 4 Cross sections for different h/H (a/b=0.37)

h/H	Section Shape	h/H	Section Shape
0.27	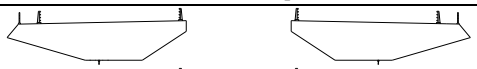	0.64	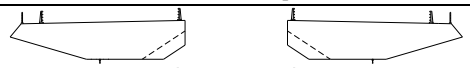
0.40		1	

Note: θ=33°, λ=90°, d/D=30%, β=66°; the width of the bottom plate changes with h/H

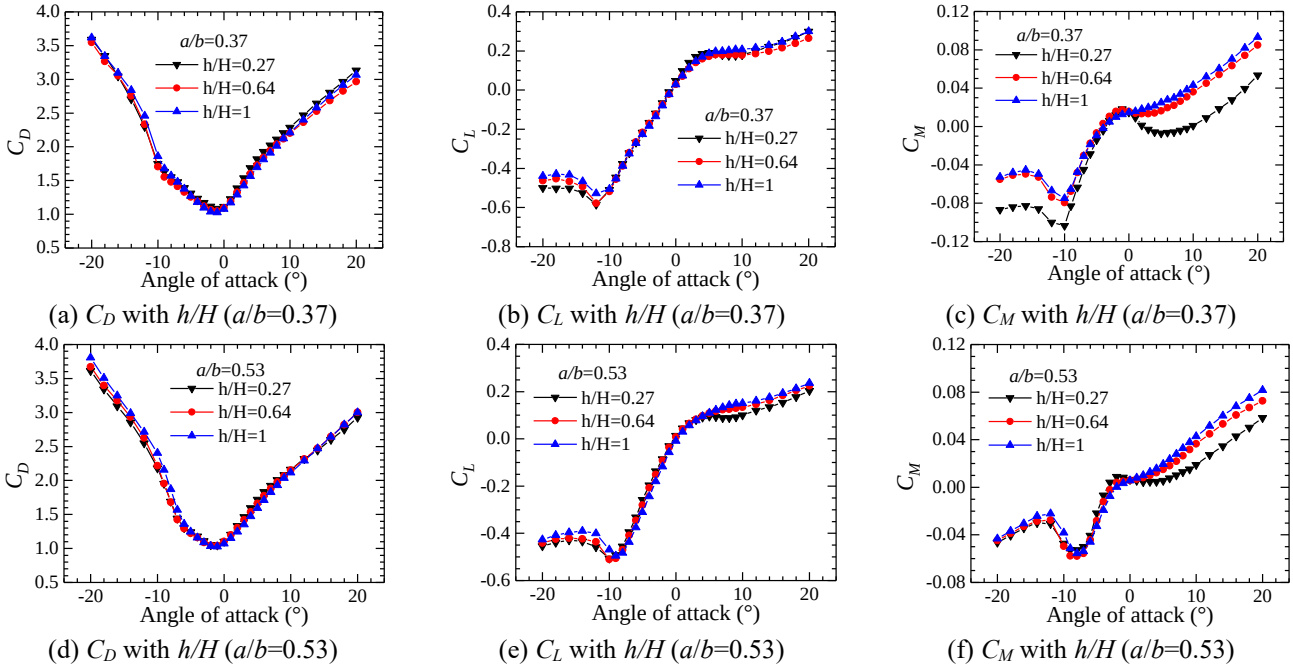

(a) C_D with h/H (a/b=0.37) (b) C_L with h/H (a/b=0.37) (c) C_M with h/H (a/b=0.37)

(d) C_D with h/H (a/b=0.53) (e) C_L with h/H (a/b=0.53) (f) C_M with h/H (a/b=0.53)

Fig. 8 Aerodynamic three-component coefficients C_L, C_D and C_M for sections with various h/H

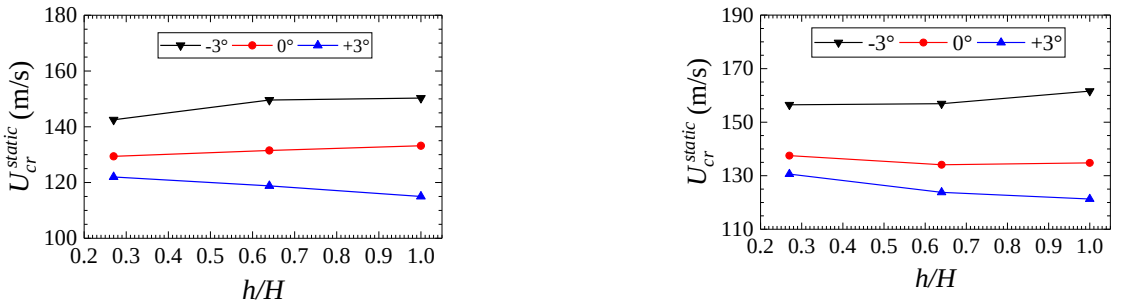

(a) Critical wind speed with h/H (a/b=0.37) (b) Critical wind speed with h/H (a/b=0.53)

Fig. 9 Critical wind speeds of wind-induced static instability for sections with various h/H

3.2.5 Influence of the inclination angle of inner lower web (θ)

Section shapes of θ =16°and 33° with a/b=0.53 are shown in Table 5. While changing θ, the width of the bottom plate was kept the same. As a result, h/H increases with θ. Sections of θ =16°, 22°, 28° and 33° were investigated with a/b set as 0.53 and 0.6, respectively.

As shown in Fig. 10, θ has little influence on C_D or C_L. Although C_M seems to decrease with the increase of θ under positive AoAs, the influence of θ on C_M is minor compared with other parameters discussed above.

For a/b=0.53 and 0.6, the minimum critical wind speed increases from 130.6 m/s and 131.6 m/s to 135.0 m/s and 137.5 m/s, respectively, with the decrease of θ as Fig. 11 shows. The decrease of θ is beneficial to the wind-induced static stability of the cable-stayed bridge. Decreasing θ will

Table 5 Cross sections for θ =16°and 33° (a/b=0.53)

θ	Section Shape
33°	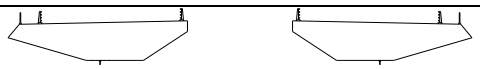
16°	

Note: λ=90°, d/D=30%, β=66°; the width of the bottom plate is fixed; h/H changes with θ

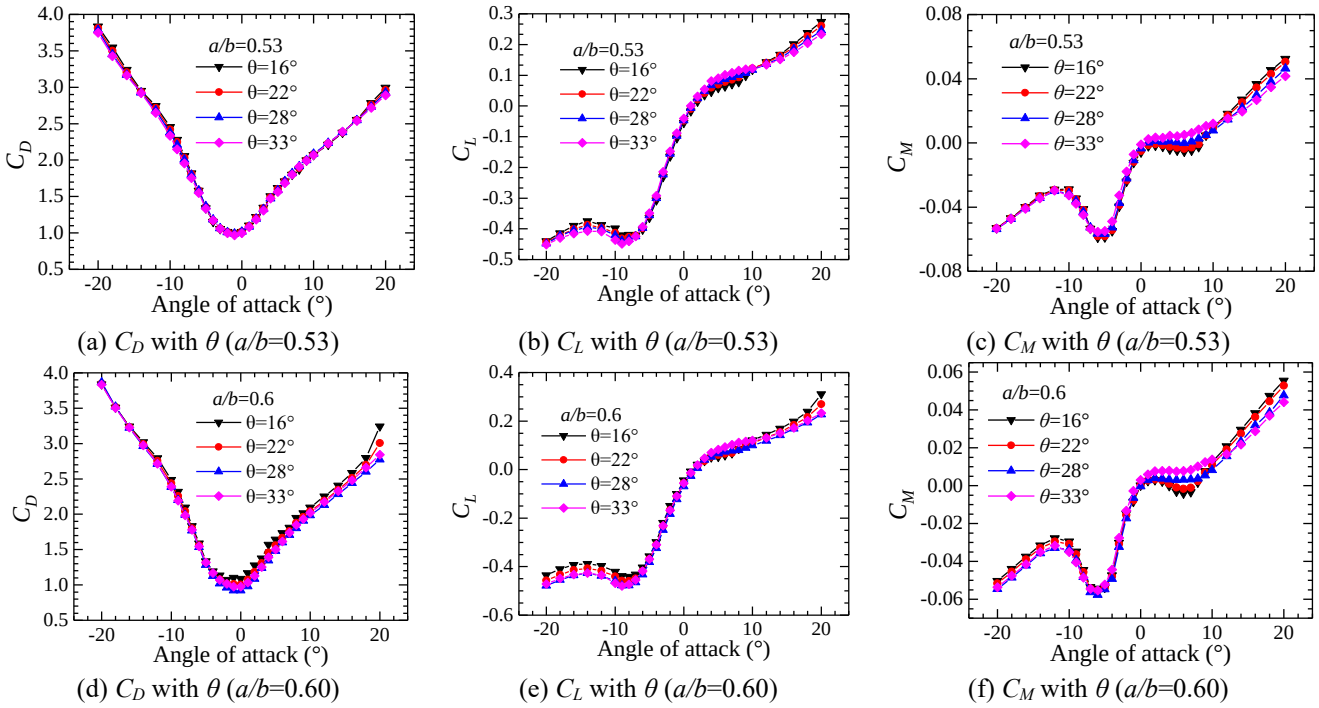

(a) C_D with θ (a/b=0.53) (b) C_L with θ (a/b=0.53) (c) C_M with θ (a/b=0.53)

(d) C_D with θ (a/b=0.60) (e) C_L with θ (a/b=0.60) (f) C_M with θ (a/b=0.60)

Fig. 10 Aerodynamic three-component coefficients C_L, C_D and C_M of for sections with various θ

(a) Critical wind speed with θ (a/b=0.53) (b) Critical wind speed with θ (a/b=0.6)

Fig. 11 Critical wind speeds of wind-induced static instability for sections with various θ

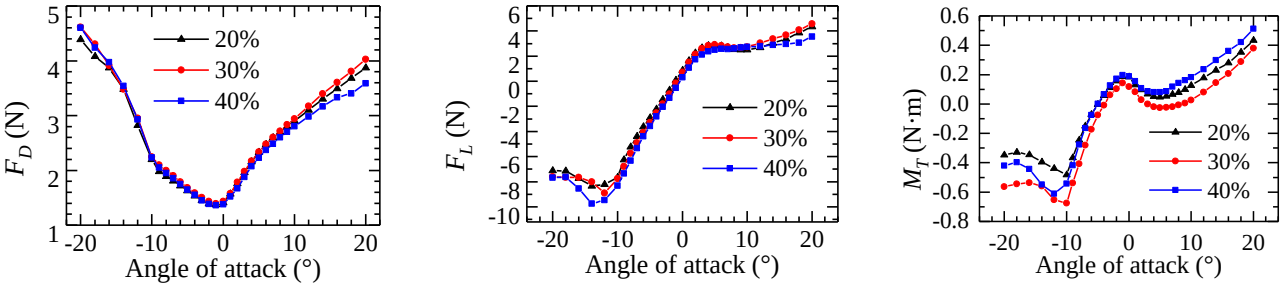

(a) Drag force (b) Lift force (c) Torsional moment

Fig. 12 Aerodynamic three-component force corresponding to sections with various d/D

increase the critical wind speed at +3° AoA, but has little effect on the critical wind speed at 0° and -3°. This is because the change of θ mainly affects C_M under positive AoAs.

3.2.6 Influence of the slotting ratio (d/D)

Based on the cross-section with a/b =0.37, h/H =0.27, and θ=33°, the aerodynamic coefficients of the sections with d/D =20%, 30% and 40% were obtained. It is worth noting that the change of the slotting rate will change the width of the section, to which the lift coefficient and torsional moment coefficient of the section are related. The aerodynamic forces instead of the force coefficients are therefore shown in Fig. 12. For positive AoAs, d/D only affects the drag and lift force when the AoA is greater than about 8°, where a 30% slotting ratio yields the highest drag

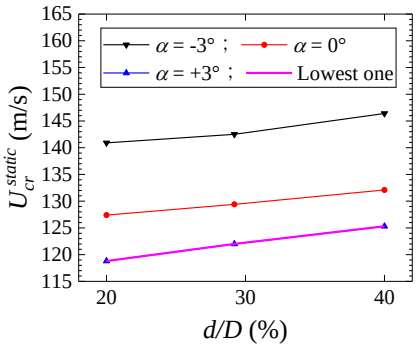

Fig. 13 Critical wind speeds of wind-induced static instability for sections with various d/D

and lift forces. The torsional moment, however, reaches the lowest values when d/D=30% and the highest value when d/D=40% for all positive AoAs.

The critical wind speeds corresponding to different d/D were computed and shown in Fig. 13. With the increase of d/D from 20% to 40%, the performance of wind-induced static stability improves for all three angles of attack, and the minimum critical wind speeds increase from 118.8 m/s to 125.3 m/s.

3.2.7 Influence of the angle of wind fairing apex (β)

Section shapes with different β are shown in Table 6. The values of β investigated are 40°, 50° and 66°. It is commonly known that a smaller β may lead to a higher flutter performance while a β larger than 66° is seldom seen in bridge designs. Fig. 14 shows the aerodynamic coefficient resulting from different β. The obvious increase of C_L and

C_M with β under positive AoAs almost certainly will have a negative influence on the static stability. Note that it is the static stability that needs to be enhanced, β should therefore stay to be 66°.

3.2.8 Summary on the parameter influence on wind-induced static instability

The influence of all four parameters on the critical wind speed is listed in Table 7. The static wind-resistant stability can be improved by raising the values of a/b or d/D, or decreasing the values of h/H or θ. However, from the perspective of engineering design, decreasing h/H while keeping θ constant will narrow the bottom plate and diminish the structural stiffness; expanding d/D will notably increase the entire width of the deck, consequently widening the towers and foundations. In this connection, it

Table 6 Cross sections for different β and λ

β	Section Shape
66°	
50°	
40°	

Table 7 Effects of shape parameters change on critical wind speed for static stability

Parameter	Variation	AoAs		
		-3°	0°	+3°
a/b	increase	increase	increase	increase
h/H	decrease	decrease	minor influence	increase
θ	decrease	minor influence*	minor influence	increase
d/D	increase	increase	increase	increase
β	decrease	--	--	increase

*: appropriate except in the case of θ=33°

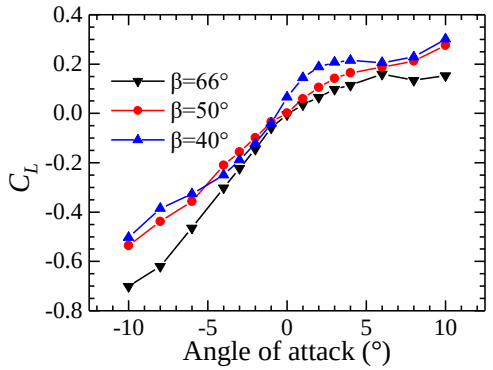

(a) Lift coefficient C_L

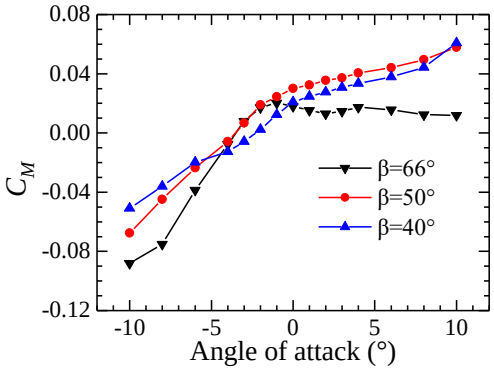

(b) Torsional moment coefficient C_M

Fig. 14 Lift coefficient C_L and torsional moment coefficient C_M for sections with various β

is suggested to focus mainly on the parameters of a/b and θ while aerodynamically optimizing the central-slotted box deck for static wind-resistant performance.

3.3 Influence of shape parameters on flutter performance

3.3.1 Sectional model test for flutter critical wind speed

To investigate the influence of shape parameters on the flutter performance, wind tunnel tests on spring-suspended sectional models were carried out in the TJ-2 Wind Tunnel. The geometric length scale is 1/80. The length, width, and height of the sectional model are 1.74 m, 0.663 m, and 0.056 m, respectively. The total equivalent mass and inertia moment of mass of the model system are 10.32 kg and 0.438 kg·m^2, respectively, for all model variations. The

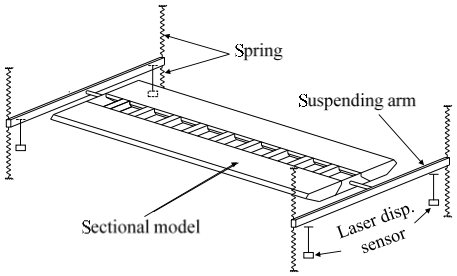

(a) Schematic diagram

(b) Sectional model mounted in TJ-2 Wind Tunnel

Fig. 15 Spring-suspended sectional model system

natural frequencies of vertical and torsional vibrations of the model system are 1.67 Hz and 4.34 Hz, respectively. The above dynamic characteristics of the sectional model system are computed according to the cross-section with d/D=30%. The torsional-vertical frequency ratio is about 2.6, which is high for long-span cable-stayed bridges with a twin-box deck. The testing wind speed ranged from 2m/s to 24 m/s, corresponding to the prototype wind speed ranging from 14.7 m/s to 175.2 m/s.

Fig. 15(a) shows a schematic diagram of the testing model system. Fig. 15(b) is a photo of the model mounted in

TJ-2 Wind Tunnel. The flutter critical wind speed for the AoAs of -3°, 0° and 3° were obtained from the tests on various section shapes.

3.3.2 Influence of shape parameters on flutter critical wind speed

According to the works presented in Subsection 3.2, the wind-resistance performance of the concerned deck against wind-induced static instability can be effectively improved by adjusting three aerodynamic shape parameters, i.e., *a/b, θ,* and *d/D.* Judging from previous experience, these three parameters may also play an important role in the against-flutter performance in which the influence of *h*/*H* is probably minor. The variations of these three parameters were therefore investigated via flutter wind tunnel tests. Tables 8-10 show the prototype flutter critical wind speeds corresponding to different deck shapes.

For a/b≥0.53, the critical wind speed for flutter at -3° AoA is the lowest, and the flutter critical wind speed decreases with the increase of *a/b*, while increases with *θ*.

Table 8 Critical wind speeds of flutter for sections with various *a*/*b* (m/s)

a/b	AoAs			Lowest critical speed
	-3°	0°	+3°	
0.37	>175.2	>175.2	161.5	161.5
0.53	134.8	>175.2	>175.2	134.8
0.56	129.7	>175.2	>175.2	129.7
0.60	126.8	>175.2	>175.2	126.8
0.67	104.5	167.2	>175.2	104.5

Note: *h*/*H*=0.27, *θ*=33°, *d*/*D*=30%, *λ*=90°, *β*=66°. The width of the bottom plate is constant

Table 9 Critical wind speeds of flutter for sections with various *θ* (m/s)

a/b	*θ*	AoAs			Lowest critical speed
		-3°	0°	+3°	
0.53	16	116.6	>175.2	>175.2	116.6
	22	126.5	>175.2	>175.2	126.5
	28	131.9	>175.2	>175.2	131.9
	33	134.8	>175.2	>175.2	134.8
0.56	16	110.3	>175.2	>175.2	110.3
	22	120.9	>175.2	>175.2	120.9
	28	126.0	>175.2	>175.2	126.0
	33	129.7	>175.2	>175.2	129.7
0.60	16	106.7	>175.2	>175.2	106.7
	22	113.9	>175.2	>175.2	113.9
	28	122.3	>175.2	>175.2	122.3
	33	126.8	>175.2	>175.2	126.8

Note: *λ*=90°, *d*/*D*=30%, *β*=66°; the width of the bottom plate keeps unchanged, and *h*/*H* changes with *θ*

Table 10 Critical wind speeds of flutter for sections with various *d*/*D* (m/s)

a/b	*d/D*	AoAs			Lowest critical speed
		-3°	0°	+3°	
0.53	20.0%	131.9	>175.2	>175.2	131.9
	30.0%	134.8	>175.2	>175.2	134.8
	40.0%	129.1	>175.2	>175.2	129.1

Note: *h*/*H*=0.27, *θ*=33°, *λ*=90°, *β*=66°. The width of the bottom plate keeps unchanged

For the influence of the slot width on the flutter, among the three slotting ratios (*d*/*D*) investigated, the flutter critical wind speed reaches the highest value when *d*/*D* is 30%.

3.4 Aerodynamic shape optimization for both wind-induced static and flutter instabilities

Based on the above discussions, the following conclusions can be drawn on the parameter influence of both wind-induced static and flutter instabilities. Although the static critical wind speed always increases with *d/D*, a *d/D* value of 30% is not only the best in relation to flutter performance but also economically reasonable, leaving *a*/*b*

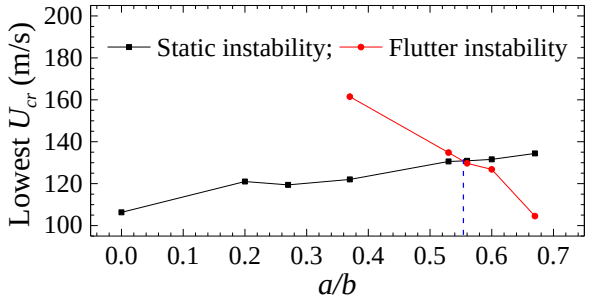

Fig. 16 Variations of critical wind speeds of static and flutter instability with a/b (h/H=0.27, θ=33°, d/D=30%, λ=90°, β=66°)

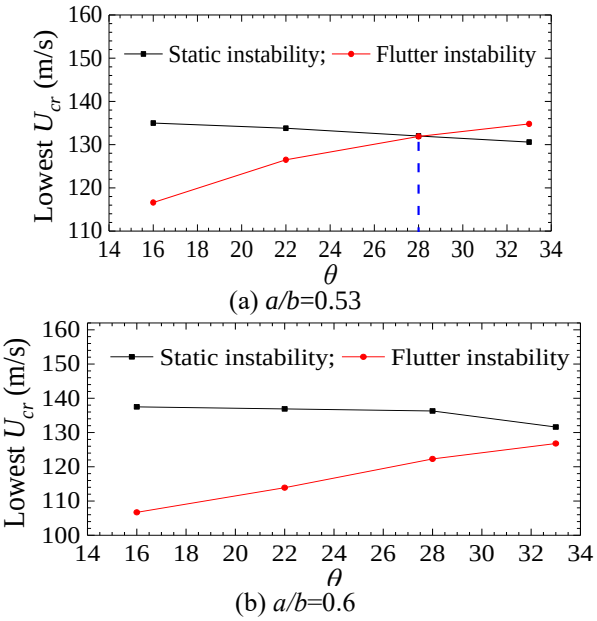

Fig. 17 Variations of critical wind speeds of flutter and wind-induced static instability with θ (d/D=30%, λ=90°, β=66°)

and θ the only crucial varying parameters for the optimization. Increasing the values of a/b or θ both have opposite effects on the static and flutter critical wind speed. Increasing a/b or decreasing θ will raise the static critical wind speed while diminishing the flutter critical wind speed.

Fig. 16 shows the variation in the critical wind speeds of both instabilities with the shape parameter a/b. With the increase of a/b, i.e., when the wind fairing apex moves down towards the bottom of the deck, the critical wind speed of flutter decreases whilst that of the wind-induced static instability rises. The slope of the flutter critical wind speed curve is much steeper than that of the static critical wind speed curve, meaning that the flutter performance of the bridge is more sensitive to the change of a/b. The two curves meet at a value of a/b of about 0.55 with a critical wind speed of about 132m/s.

Fig. 17 shows the variations of the critical wind speeds of flutter and wind-induced static instability with θ. With the increase of θ, namely, when the slope of the inner lower web decreases, the critical wind speed of the flutter rises

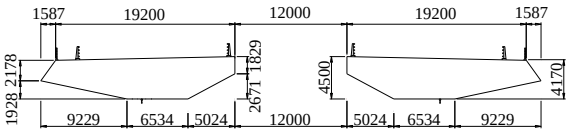

Fig. 18 Diagram of optimized section (unit: mm)

whilst the critical wind speed of wind-induced static instability decreases. The flutter critical wind speed is a little more sensitive to θ than the static critical wind speed. In the case of a/b=0.53, the two curves meet at a θ of about 28° with a wind speed of about 132 m/s. In the case of a/b=0.60, the critical wind speed of static instability keeps being higher than that of flutter, and the flutter critical wind speed, in this case, is lower than the case of a/b=0.53.

The above results show that a/b=0.53, θ=28° are preferable values for the two parameters with the highest general critical wind speed (the lower one between the two) of about 132 m/s. The optimal deck shape is shown in Fig. 18 with the other shape parameters being d/D=30%, h/H=0.41, λ=90° and β=66°.

4. VIV countermeasures

Central-slotted decks are prone to VIV (Dragomirescu *et al.* 2016, Larsen *et al.* 2008, Li *et al.* 2018, Yang *et al.* 2015a). In addition to the above optimization, the VIV performance of the section must be investigated. As the effects of VIV countermeasures highly depend on the shape of the section, such investigation should be conducted after the optimization based on static and flutter aerodynamics.

The VIV test device and model are generally consistent with the flutter test described in Subsection 3.3.1 only with different dynamic characteristics. The total equivalent mass and inertia moment of mass of the model system are 15.39 kg and 0.748 kg·m^2, respectively. The natural frequencies of vertical and torsional vibrations of the model system are 3.37 Hz and 8.06 Hz, respectively. For super-long span cable-stayed bridges, the damping ratio is usually lower than 0.5%. Therefore, from a conservative perspective, the damping ratios of vertical bending and torsion were both set as 0.3% which were adjusted by viscous damper and constant for all experiment cases.

The Scruton numbers of the model and the prototype bridge are 13.81 and 9.18, respectively. Therefore, the VIV responses of the sectional model discussed were converted into those of the prototype bridge for convenience using the method introduced by Zhu (2005).

The name, shape and position of the countermeasures investigated are shown in Fig. 19. First, the effects of the countermeasures on the section shown in Fig. 19 were investigated separately as listed in Table 11.

The VIV responses of the sections listed in Table 11 are shown in Fig. 20.

For vertical VIV, the installation of wind barriers (sec7) reduces the peak amplitude from 0.27 m to 0.16 m. The improvements shown in sec2, sec5, and sec6, are quite limited. Moving the maintenance track inward (sec3) or installation of the maintenance track guide plate (sec6) have

negative effects.

to 0.45° and 0.44°, respectively.

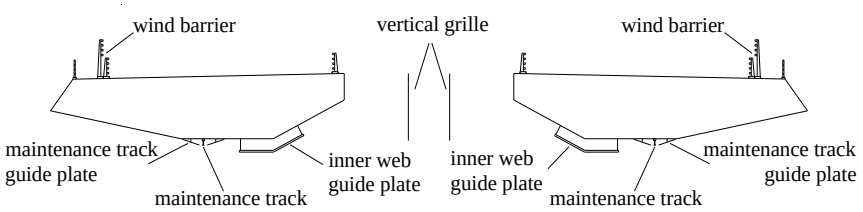

(a) VIV suppression measures

(b) Vertical grilles with 50% porosity

Fig. 19 Schematic diagram of VIV suppression measures

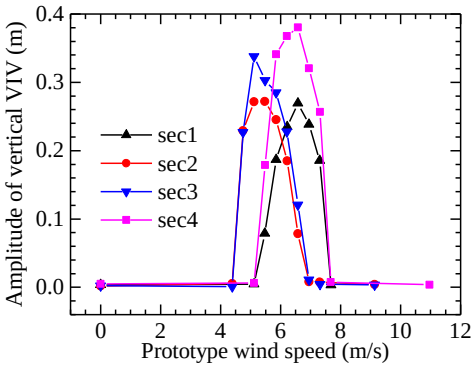

(a) Amplitude of vertical VIV (sec1-sec4)

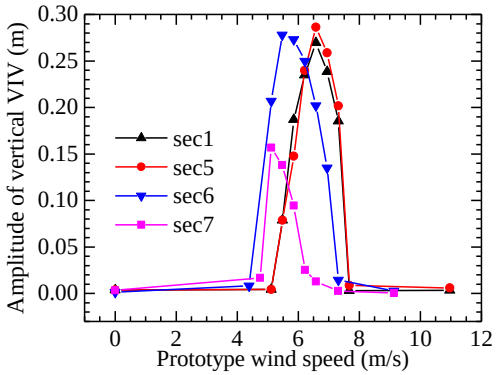

(b) Amplitude of vertical VIV (sec1, sec5-sec7)

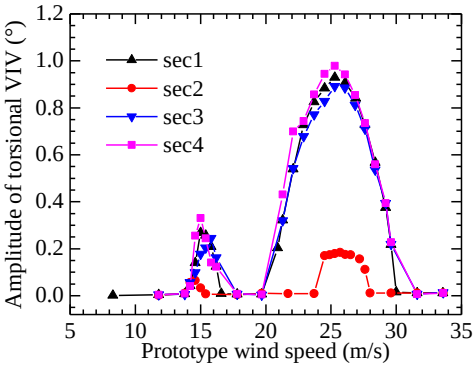

(c) Amplitude of torsional VIV (sec1-sec4)

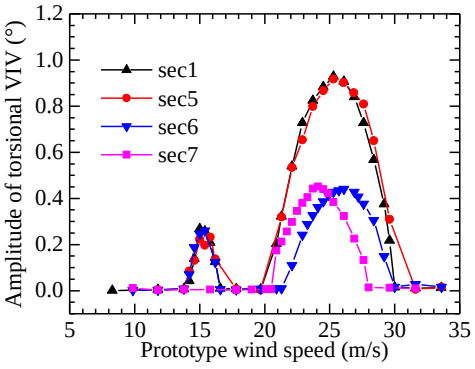

(d) Amplitude of torsional VIV (sec1, sec5-sec7)

Fig. 20 VIV amplitude of section installed with measure at +3°

Table 11 Section numbers corresponding to separate countermeasures

Section number	Measures	Section number	Measures
sec1	none	sec5	vertical grilles with 50% ventilation
sec2	remove maintenance track	sec6	inner web guide plate
sec3	moving maintenance track inwards	sec7	wind barrier
sec4	add maintenance track guide plate		

For torsional VIV, sec 3, sec 4 and sec5 show little difference in the VIV responses from the original section. The removal of the maintenance track (sec2) eliminates the first lock-in range (low-wind-speed VIV) and reduces the peak response in the second lock-in range (low-wind-speed VIV) from 0.93° to 0.18°. Adding the wind barrier (sec 7) or the inner web guide plates (sec6) also eliminate the first lock-in range and reduced the peak amplitude in the second

To further reduce the VIV responses, a series of combinations of the above measures were tested. The sections with the combined measures are listed in Table 12.

The VIV responses of the sections listed are presented in Fig. 21.

For vertical VIV, sec 8 and 9 show worse VIV performance than the original section. Sec 10~13 have smaller responses than the original section. Among these sections, sec 11 with wind barriers and inner web guide

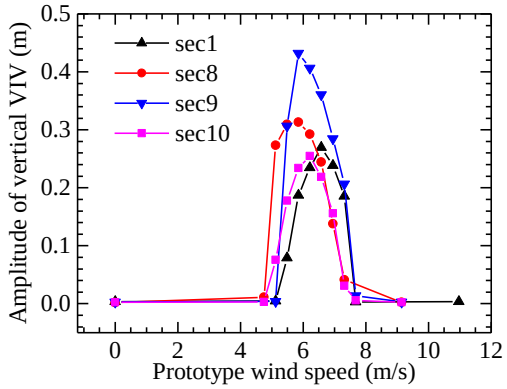

(a) Amplitude of vertical VIV (sec1, sec8-sec10)

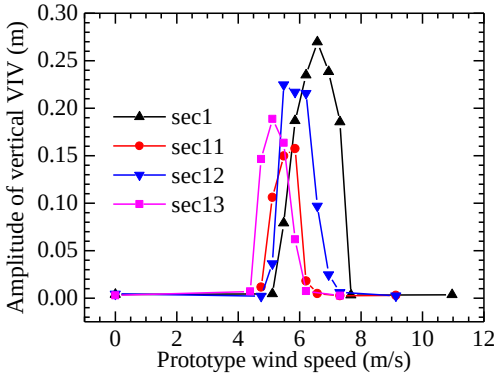

(b) Amplitude of vertical VIV (sec1, sec11-sec13)

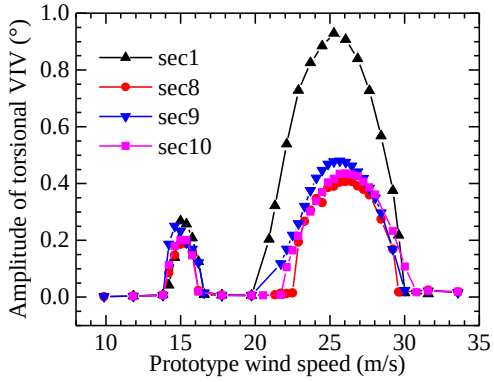

(c) Amplitude of torsional VIV (sec1, sec8-sec10)

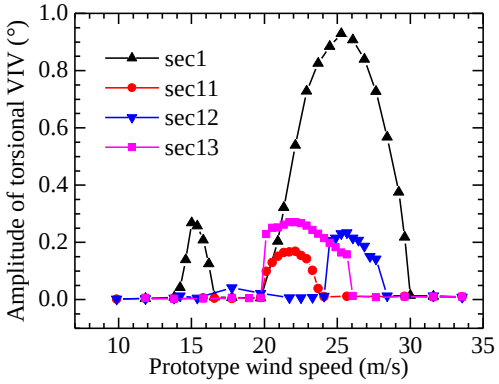

(d) Amplitude of torsional VIV (sec1, sec11-sec13)

Fig. 21 VIV amplitude of section installed with combined measures at +3°

Table 12 Section number corresponding to measures combination

Section Number	Measure Combination
sec8	moving maintenance track inwards + inner web guide plate
sec9	maintenance track guide plate + inner web guide plate
sec10	vertical grille in the slot + inner web guide plate
sec11	wind barrier + inner web guide plate
sec12	remove maintenance track+ inner web guide plate
sec13	moving maintenance track inwards + wind barrier + inner web guide plate

plates harbours the smallest vertical amplitude of about 0.16 m, which is similar to installing the wind barriers alone. Vertical vibration amplitude of 0.16 m corresponds to the acceleration of 0.15 m/s^2.

For torsional VIV, all the combinations show remarkable improvements from the original section. Sec 11 exhibit the best VIV performance by eliminating the first lock-in range and reducing the peak amplitude in the second from 0.93° to 0.17°. This is a remarkable further improvement compared with installing the wind barriers or guide plates alone.

5. Aerodynamic performance with the optimized section

Taking into account the wind-induced static stability, flutter and VIV performance, the comprehensively optimized section VIV countermeasures are shown in Fig. 22. It should be noted that first, the performance of the above section against wind-induced static and flutter instability can change after the installation of the VIV countermeasures, so the procedures for the determination of critical wind speeds should be conducted again for the final results. Second, the critical wind speed for static instability is established through full-bridge analyses while that for the

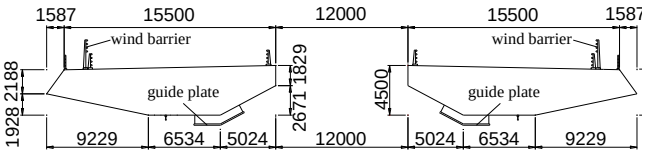

Fig. 22 Diagram of the final section with VIV suppression measures (unit: mm)

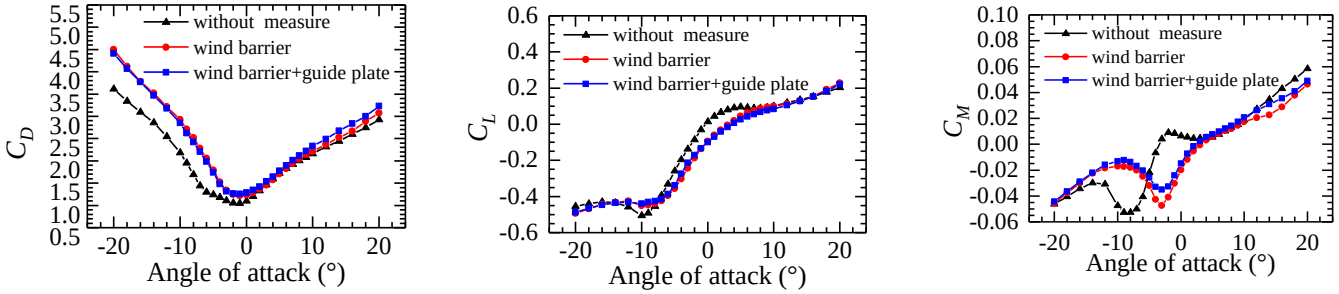

Fig. 23 Aerodynamic coefficients of sections with/without VIV countermeasures

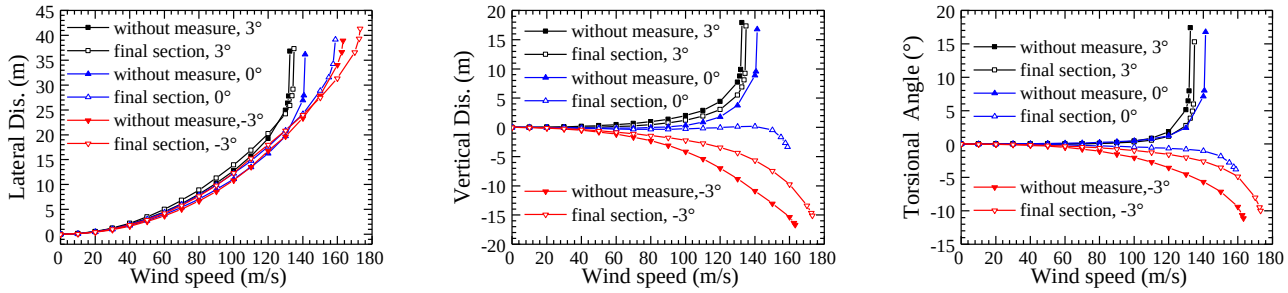

(a) Lateral (b) Vertical (c) Torsional

Fig. 24 Displacement variations at mid-span

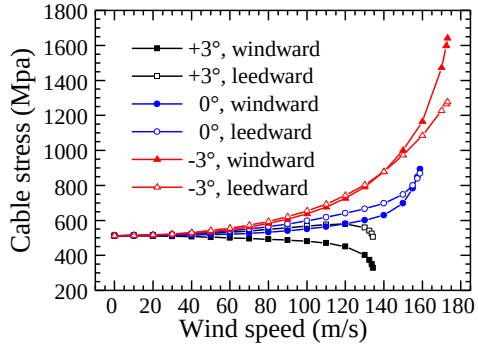

Fig. 25 Cable stress variations at mid-span

flutter instability is obtained via sectional wind tunnel tests, a flutter analysis on the finite element model of the bridge is needed for the results to be compatible.

5.1 Analysis of wind-induced static instability

The aerodynamic coefficients of the optimized sections with/out VIV countermeasures are shown in Fig. 23. The wind barriers have a large influence on the coefficients, while the installation of the guide plates has little effect on the coefficients. The wind barriers considerably increase C_D under negative AoAs and slightly increase C_D under positive AoAs. Wind barriers reduce C_L under AoAs ranging from -10° to 10°. C_M shows significant changes with the wind barriers under AoAs below 3°: C_M now increase from negative to positive under much larger AoAs.

The nonlinear wind-induced static instability analyses of the 1400 m main-span cable-stayed bridge with the optimized sections were then conducted. The VIV countermeasures provide a performance enhancement under all AoAs, with critical wind speeds at AoAs of -3°, 0° and 3° increasing from 163.1 m/s, 141.3 m/s and 132 m/s to 173.1 m/s, 158.8 m/s and 134.4 m/s. Fig. 24 shows the variations of lateral, vertical and torsional displacements of the bridge deck at the mid-span with the increase of wind speed for AoAs of -3°, 0° and 3°. For the final optimal section, the static instability occurs with the torsional deformations at the mid-span of 15.3°, -3.8° and -10.0° for AoAs of +3°, 0° and -3°, respectively. The corresponding lateral displacements are 37.3m°, 39.2m and 41.4m, respectively and the vertical displacements are 17.3m, -3.3m and -15.1m, respectively. Fig. 25 shows the variations of cable stress at the mid-span with the increase of wind speed for AoAs of -3°, 0° and 3°. For AoAs of 0° and -3°, stresses of both the windward and leeward cables increase with the increase of the wind speed. For AoAs of +3°, the cable stress of the windward side decreases with the increase of wind speed due to the upward and torsional movement of the deck, while the cable stress of the leeward side first increases due to the torsion and then decreases when the deck approaches instability.

5.2 Three-dimensional nonlinear flutter analysis

The full-bridge flutter analyses of the final schemes of the super-long span cable-stayed bridges were carried out a hybrid-frequency-time domain flutter analyses method proposed by Hua *et al.* (2007). The method utilizes matrix elements to model the aeroelastic stiffness and damping acting on the bridge, expressed in terms of the reduced wind velocity and flutter derivatives. Damped complex eigenvalue analyses can therefore be conducted to determine the critical wind speed. For a given wind

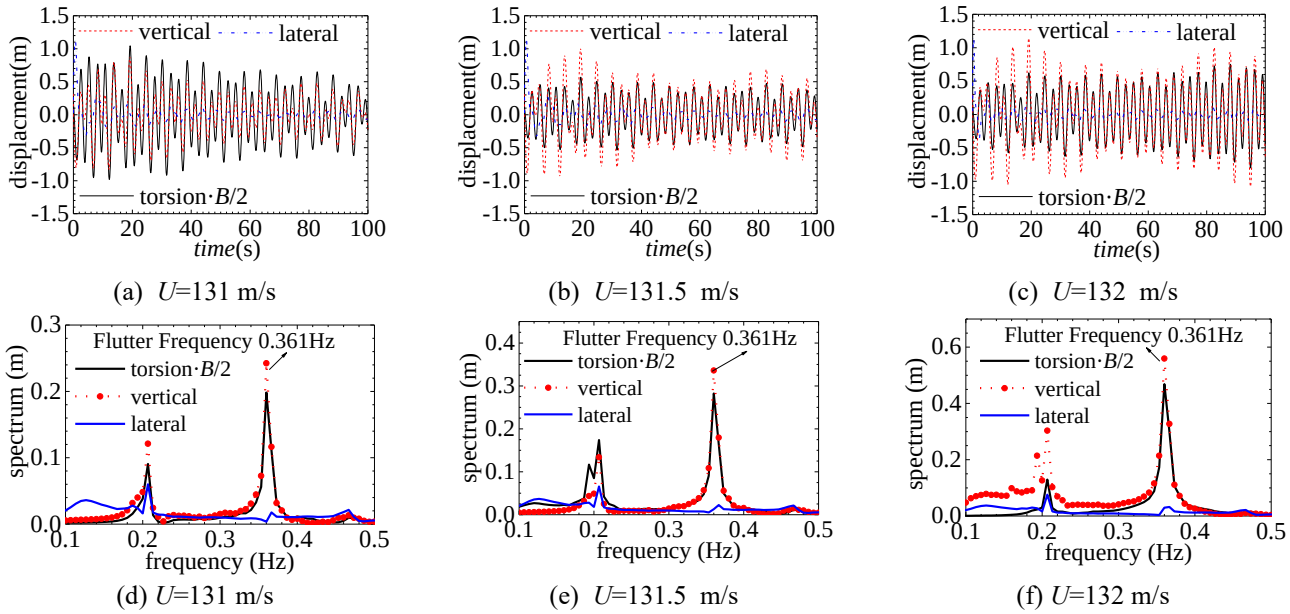

(a) U=131 m/s (b) U=131.5 m/s (c) U=132 m/s

(d) U=131 m/s (e) U=131.5 m/s (f) U=132 m/s

Fig. 26 Displacement time history and spectrum at mid-span near flutter critical wind speed (-3°)

Table 13 Critical wind speeds of the final scheme

AoA/°	Critical wind speed (m/s)			Dominant instability type
	wind-induced static instability	flutter	minimum	
-3	173.1	131.5	131.5	flutter
0	158.7	>158.7	158.7	wind-induced static instability
+3	134.4	>134.4	134.4	wind-induced static instability

velocity, time-domain responses of the system subjected to an initial excitation can be computed using a time integration scheme. Wind tunnel sectional model tests with AoAs between ±10° were conducted for the acquisition of the aerodynamic derivatives (Zhu *et al*. 2019). The effects of large deformation and stress-stiffening effects are considered in the full-bridge flutter analyses.

As the wind-induced static analyses are embedded in the time-frequency-domain flutter analyses, when the static instability occurs before the flutter under 0° and 3° AoAs, the critical wind speed of the flutter cannot be obtained. This does not affect the overall results as the -3° AoA has the dominating critical wind speed.

Fig. 26 shows the displacement time-histories and spectra at the mid-span as the wind speed approaches the critical at the AoA of -3°. When the wind speed increases from 131 m/s to 132 m/s, the torsional displacement evolves from decaying to stable oscillation, then to slow divergence. The critical wind speed of the flutter can then be determined as around 131.5 m/s. The displacement spectra show that the responses in all directions contain multiple frequency components, among which the first-order torsional frequency component accounts for the largest proportion.

The flutter analysis was carried out after the static analyses, and the modal shape is coupled between vertical, torsional and lateral DOFs. The time-frequency domain algorithm is adopted in the flutter analysis with the reduced frequencies manually assigned for flutter derivatives. Therefore, the 0.2 Hz component shown in the figure is a pseudo-mode produced in the process.

Table 13 shows the critical wind speeds of the final scheme under all three AoAs. The dominant critical wind speed of the super-long span bridge with the aerodynamically optimized deck can reach about 131.5 m/s, which shows about an 8% rise from the preliminary design.

6. Conclusions

This study concerns improvements of the aerodynamic stability of a super-long span cable-stayed bridge with a central-slotted box deck of which the preliminary design has a critical wind speed for wind-induced static instability far lower than that of flutter. To this end, the influence of a series of deck shape parameters on both static and flutter instabilities has been investigated and discussed. Some crucial shape parameters, like the height ratio of wind fairing (a/b) and the angle of the inner-lower web (θ), show opposite influences on the two kinds of instability.

The aerodynamic shape optimization conducted for both static and flutter instabilities on the deck based on the above parameter-sensitivity study proposes a bridge scheme with close critical wind speeds for the static and flutter instabilities, and raises the overall critical wind speed by about 8%. Effective VIV countermeasures for this type of bridge deck have also been proposed by this study.

Acknowledgments

The work described in this paper was jointly supported by the National Natural Science Foundation of China (Grant 51938012) and the Fundamental Research Fund for State

Key Laboratories from the Ministry of Science and Technology of China (SLDRCE19-A-15), for which the authors are very grateful. The authors also would like to express their appreciation to Prof. Rucheng Xiao, Dr. Bin Sun and their graduate students, Ms Cong Wang from the Department of Bridge Engineering of Tongji University, for the preliminary design of the super-long cable-stayed bridges investigated in this study.

References

Boonyapinyo, V., Yamada, H. and Miyata, T. (1994), "Wind-induced nonlinear lateral-torsional buckling of cable-stayed bridges", *J. Struct. Eng. - ASCE*, **120**(2), 486-506. https://ascelibrary.org/doi/10.1061/(ASCE)0733445(1994)120:2(486).

Cheng, J., Jiang, J.J., Xiao, R.C. and Xiang, H.F. (2002), "Advanced aerostatic stability analysis of cable-stayed bridges using finite-element method", *Comput. Struct.*, **80**(13), 1145-1158. https://doi.org/10.1016/S0045-7949(02)00079-2.

Dragomirescu, E., Wang, Z.D. and Hoftyzer, M.S. (2016), "Aerodynamic characteristics investigation of Megane multi-box bridge deck by CFD-LES simulations and experimental tests", *Wind Struct.*, **22**(2), 161-184. https://doi.org/10.12989/was.2016.22.2.161

Gimsing, N.J., Georgakis, C.T. (2012), *Cable Supported Bridges: Concept and Design (3rd Ed.)*, John Wiley & Sons, New York, N.Y.

Hirai, A., Okauchi, I., Ito, M. and Miyata, T. (1967), "Studies on the critical wind velocity for suspension bridges", *Proceeding of the International Research Seminar on Wind Effects on Buildings and Structures*, Ontario, Canada,

Hu, C.X., Zhou, Z.Y. and Jiang, B.S. (2019), "Effects of types of bridge decks on competitive relationships between aerostatic and flutter stability for a super long cable-stayed bridge", *Wind Struct.*, **28**(4), 255-270. https://doi.org/10.12989/was.2019.28.4.255.

Hua, X.G., Chen, Z.Q., Ni Y.Q. and Ko, J.M. (2007), "Flutter analysis of long-span bridges using ANSYS", *Wind Struct.*, **10**(1), 61-82. https://doi.org/10.12989/was.2019.28.4.255.

Jiang, B., Zhou, Z., Yan, K. and Hu, C. (2019), "Aerodynamic Performance of Bridge with Typical Box Girder Sections at Different Web Inclinations", *J. Tongji Univ.. Natural Sci.*, **47**(8), 1106-1114(in Chinese).

Kien, P.H., Yamada, H., Katsuchi, H. and Sasaki, E. (2007), "Study on wind-induced instability of Super Long-Span Cable-Stayed Bridge", *J. Struct. Eng. A*, **53**, 650-657.

Larsen, A. (1993), "Aerodynamic aspects of the final design of the 1624 m suspension bridge across the Great Belt", *J. Wind Eng. Ind. Aerod.*, **48**(2-3), 261-285. https://doi.org/10.1016/0167-6105(93)90141-A.

Larsen, A. and Astiz, M.A. (1998), "Aeroelastic consideration for the Gibraltar Bridge feasibility study", *Bridge Aerodynamics. Rotterdam: Balkema*, 165-173.

Larsen, A., Savage, M., Lafrenière, A., Hui, M. and Larsen, S.V. (2008), "Investigation of vortex response of a twin box bridge section at high and low Reynolds numbers", *J. Wind Eng. Ind. Aerod.*, **96**(6-7), 934-944. https://doi.org/10.1016/j.jweia.2007.06.020.

Li, H., Laima, S., Ou, J., Zhao, X., Zhou, W., Yu, Y., Li, N. and Liu, Z. (2011), "Investigation of vortex-induced vibration of a suspension bridge with two separated steel box girders based on field measurements", *Eng. Struct.*, **33**(6), 1894-1907. https://doi.org/10.1016/j.engstruct.2011.02.017.

Li, Z.G., Zhou, Q., Liao, H.L. and Ma, C.M. (2018), "Numerical studies of the suppression of vortex-induced vibrations of twin box girders by central grids", *Wind Struct.*, **26**(5), 305-315. https://doi.org/10.12989/was.2018.26.5.305.

Liu, S., Zhao, L., Fang, G., Hu, C. and Ge, Y. (2021), "Investigation on aerodynamic force nonlinear evolution for a central-slotted box girder under torsional vortex-induced vibration", *J. Fluid. Struct.*, **106**. https://doi.org/10.1016/j.jfluidstructs.2021.103380.

Nagai, M., Fujino, Y., Yamaguchi, H. and Iwasaki, E. (2004), "Feasibility of a 1,400 m span steel cable-stayed bridge", *J. Bridge Eng.*, **9**(5), 444-452.

Qian, C., Zhu, L., Zhu, Q., Ding, Q. and Yan, L. (2022), "Pattern and mechanism of wind-induced static instability of super-long-span cable-stayed bridge under large deformation", *J. Wind Eng. Ind. Aerod.*, **221**, 104910. https://doi.org/10.1016/j.jweia.2022.104910.

Sato, H., Hirahara, N., Fumoto, K., Hirano, S. and Kusuhara, S. (2002), "Full aeroelastic model test of a super long-span bridge with slotted box girder". *J. Wind Eng. Ind. Aerod.*, **90**(12), 2023-2032. https://doi.org/10.1016/S0167-6105(02)00318-5.

Sato, H., Kusuhara, S., Ogi, K. and Matsufuji, H. (2000), "Aerodynamic characteristics of super long-span bridges with slotted box girder", *J. Wind Eng. Ind. Aerod.*, **88**(2-3), 297-306. https://doi.org/10.1016/s0167-6105(00)00055-6.

Yang, Y., Ge, Y. and Xiang, H. (2007), "Flutter control effect and mechanism of central-slotting for long-span bridges", *Frontiers of Architecture and Civil Engineering in China*, **1**(3), 298-304.

Yang, Y., Zhang, L., Ding, Q. and Ge, Y. (2018), "Flutter performance and improvement for a suspension bridge with central-slotted box girder during erection", *J. Wind Eng. Ind. Aerod.*, **179**, 118-124. https://doi.org/10.1016/j.jweia.2018.05.016.

Yang, Y.X., Ma, T.T. and Ge, Y.J. (2015a), "Evaluation on bridge dynamic properties and VIV performance based on wind tunnel test and field measurement", *Wind Struct.*, **20**(6), 719-737. https://doi.org/10.12989/was.2015.20.6.719.

Yang, Y.X., Zhou, R., Ge, Y.J., Mohotti, D. and Mendis, P. (2015b), "Aerodynamic instability performance of twin box girders for long-span bridges", *J. Wind Eng. Ind. Aerod.*, **145**, 196-208. https://doi.org/10.1016/j.jweia.2015.06.014.

Zhang, X.J. and Sun, H.L. (2014), "Study of the aerostatic and aerodynamic stability of super long-span cable-stayed bridges", *Eng. Sci.*, **2**, 82-92.

Zhu, L.D. (2005), "Mass simulation and amplitude conversion of bridge sectional model test for vortex-excited resonance", *Eng. Mech.*, **22**(5), 6 (in Chinese).

Zhu, L.D., Zhang, H.J., Guo, Z.S. and Hu, X.H. (2011), "Flutter performance and control measures of a 1400m-span cable-stayed bridge scheme with steel box deck", *Proceedings of the 13th International Conference on Wind Engineering*, Amsterdam, The Netherlands, June.

Zhu, Q., Chen, W., Zhu, L. and Cui, Y. (2019), "Flutter performance of a super-long-span cable-stayed bridge under large attack angles via wind tunnel sectional model tests", *China J. Highway Transport*, **32**(10), 67-74 (in Chinese).

FR